NASA TM X-615

NASA TM X-615

TECHNICAL MEMORANDUM

X-615

INVESTIGATION OF THE STATIC STABILITY CHARACTERISTICS OF A REENTRY SPACECRAFT MODEL IN FREE FLIGHT FOR MACH NUMBERS FROM 2.62 TO 1.11 LAUNCHED AT AN ANGLE OF ATTACK OF 180°

By J. W. Usry

Langley Research Center
Langley Air Force Base, Va.

NATIONAL AERONAUTICS AND SPACE ADMINISTRATION
WASHINGTON [redacted] December 1961

1G

NATIONAL AERONAUTICS AND SPACE ADMINISTRATION

TECHNICAL MEMORANDUM X-615

INVESTIGATION OF THE STATIC STABILITY CHARACTERISTICS OF A REENTRY SPACECRAFT MODEL IN FREE FLIGHT FOR MACH NUMBERS FROM 2.62 TO 1.11 LAUNCHED AT AN ANGLE OF ATTACK OF 180°*

L 1 2 3 0

By J. W. Usry

SUMMARY

A small-scale model of a proposed manned reentry spacecraft configuration was tested in free flight to determine whether it would recover from an intentionally induced tumbling motion. The model was propelled by a two-stage launch vehicle with its rear end forward. Results indicate that the model rotated to the nose forward position and continued to oscillate through large angles of attack throughout the test period. The oscillations ranged from angles of attack of about ±160° at a separation Mach number of 2.62 to angles of attack of about ±140° at a Mach number of 1.11. The model was statically stable about the trim point for all Mach numbers and angles of attack.

INTRODUCTION

The National Aeronautics and Space Administration is devoting considerable effort to the design of spacecraft configurations suitable for manned reentry. Numerous wind-tunnel tests have been performed to determine the lift, drag, and stability on blunt, nonlifting bodies which could be used for this purpose. (For example, see refs. 1 to 9.) One of the problems associated with reentry is the turnaround maneuver which the vehicle must perform in the event of an abort during the boost phase. Unpublished motion-simulation studies (based on experimental derivatives from wind-tunnel tests) have indicated that some reentry body shapes, similar to the model reported herein, experienced oscillations of large amplitude particularly in the lower supersonic speed regime. In some cases the oscillations evolved into a complete tumbling motion.

*Title, Unclassified.

Reference 2 presents the results of an investigation of the aerodynamic characteristics of the escape and reentry configurations of the Mercury capsule in the Langley 8-foot transonic pressure tunnel. The aerodynamic characteristics of the escape, exit, and reentry configurations in the supersonic speed regime are presented in reference 3. In reference 9, a full-scale abort-escape system utilizing an escape tower was flight-tested to determine its ability to function properly in case of launch vehicle malfunction at or near take-off. Additional aerodynamic data for reentry shapes - lifting, nonlifting, and airplane-like bodies - are presented in references 4 and 5.

A flight test has been conducted to determine whether a small-scale model of a proposed manned-reentry spacecraft configuration, without the escape-tower system, would recover from an intentionally induced tumbling motion. The induced motion was imposed by separating the spacecraft from the launch vehicle at an angle of attack of 180°, which is an unstable attitude. The results of the test are reported herein.

Since the spacecraft is a body of revolution, stability about the transverse and vertical axes should be the same. In this report the static longitudinal stability is discussed; therefore, the data are presented as variations of normal-force, pitching-moment, and axial-force coefficients with the angle of attack. Data are presented for Mach numbers varying from 2.62 to 1.11 and corresponding Reynolds numbers from 5.68×10^6 to 2.10×10^6, based on the maximum cross-sectional diameter.

SYMBOLS

The aerodynamic force and moment data are referred to the body axes which have the origin at the center of gravity. (See fig. 1.) The symbols used are defined as follows:

a	acceleration, g units
C_1, C_2	constants of integration
C_A	axial-force coefficient, positive in positive X-direction, $\frac{W/S}{q} a_{l,cg}$
C_m	pitching-moment coefficient, $\frac{I_Y}{qSd} \ddot{\theta}$

C_N	normal-force coefficient, negative in positive Z-direction, $\frac{W/S}{q} a_{n,cg}$
C_n	yawing-moment coefficient, $\frac{I_Z}{qSd} \ddot{\psi}$
C_Y	transverse-yaw force coefficient, positive in positive Y-direction, $\frac{W/S}{q} a_{t,cg}$
d	maximum cross-sectional diameter of the spacecraft, ft
g	acceleration due to gravity, 32.2 ft/sec^2
I_X, I_Y, I_Z	moments of inertia about the X-, Y-, and Z-axes, slug-ft^2
M	Mach number
q	dynamic pressure, lb/sq ft
R	Reynolds number based on the maximum cross-sectional diameter
S	maximum cross-sectional area of the model, sq ft
t	time, sec
W	weight of the model, lb
x	distance along the body X-axis from the center of gravity to the normal or transverse accelerometer, positive forward, ft
x_{cg}	distance from nose of model to center of gravity, ft
x_{cp}	distance from nose of model to center of pressure, ft
X,Y,Z	body coordinate axes
α	angle of attack, deg
ϵ	angular orientation of total pitch plane, deg
θ	pitch angle, deg or radians
ϕ	roll angle, deg or radians

ψ yaw angle, deg or radians

Subscripts:

cg	center of gravity
i	indicated
l	longitudinal
n	normal
t	transverse
tot	total

A dot above a symbol indicates the first derivative with respect to time, and two dots over a symbol represent the second derivative with respect to time; for example, $\dot{\theta} = \frac{\partial \theta}{\partial t}$ and $\ddot{\theta} = \frac{\partial^2 \theta}{\partial t^2}$.

MODEL AND TEST PROCEDURE

Model

A sketch of the model is shown in figure 2 and the three-quarter front view and three-quarter rear view are shown in figure 3. The model nose section was a spherical segment with a radius of 15.75 inches. The body center section was an inverted cone with a semivertex angle of 15.4° and the afterbody was a hemisphere-cylinder-cone combination. The nose section was constructed of a mild steel and the midsection and afterbody, of Inconel. The total length of the model was 14.27 inches and the maximum cross-sectional diameter was 10.5 inches. The moments of inertia in pitch and yaw were 0.19 and in roll was 0.08 slug-ft^2. The center of gravity was located 31.1 percent of the maximum diameter aft of the geometric center of the nose along the X body axis. The total weight of the model including instrumentation was 70.5 pounds.

Test Procedure

The flight test was conducted at the NASA Wallops Station. The model was mounted on the launch vehicle with its aft end forward. The model and launch vehicle, shown in figure 4, were launched at an angle of elevation of 70°. Propulsion to test conditions was accomplished

with a two-stage, solid-fuel, launch-vehicle combination. The first stage, which was a Nike M5 rocket motor, was equipped with standard Nike fins, 5 square feet per panel, for stabilization; and the second stage, which was a Recruit XM19 rocket motor, was flare stabilized. The second stage had a high drag-to-weight ratio at burnout, relative to the model, which aided in separation of the launch vehicle from the model. The model was attached to the Recruit by an explosive bolt (0.6 of an inch in diameter).

The model was equipped with an NASA six-channel telemeter. Longitudinal, normal, and transverse acceleration data were transmitted from the spacecraft to a ground receiving station. One transverse and one normal accelerometer were located in the cylindrical portion of the afterbody and one transverse, one normal, and one longitudinal accelerometer were located in the midsection near the center of gravity. A pressure orifice was located about 2 inches from the geometric center of the blunt nose and measurements of the pressure were transmitted to the ground receiving station. The model was tracked with the FPS-16 and SCR-584 radar sets. The velocity of the model was obtained by differentiating the time-history variation of altitude and elevation angle and resolving the components along the flight path. Velocity was also computed with the measured pressure data and ambient atmosphere data and served as a check on the differentiation process.

Data were obtained during the deceleration portion of the flight as the model ascended from 35,000 to 40,000 feet. Atmospheric conditions were obtained from a rawinsonde balloon launched just prior to the test. Test conditions for the flight are shown in figure 5. The dashed portions of the curves indicate the regions applicable to the results presented in this report.

ACCURACY

The maximum instrument inaccuracies, based on ±2 percent of the calibrated range, are stated in coefficient form for representative Mach numbers in the following table:

	M = 2.62	M = 1.54	M = 1.11
C_N	±0.028	±0.093	±0.197
C_A	±0.066	±0.217	±0.461

A comparison of the axial-force coefficient with wind-tunnel data indicates the accuracy is better than that indicated in the table, especially at $M = 1.11$.

The accuracy of the angle of attack is difficult to assess. General consideration of the data-reduction technique and comparison with wind-tunnel data indicate the maximum inaccuracy is $\pm 10^{\circ}$.

ANALYSIS

Force coefficients.- The normal- and axial-force coefficients were calculated from the acceleration of the center of gravity of the model. Equations (1), (2), and (3) of reference 10 show the expressions necessary for correcting accelerations to the center of gravity. If the accelerometers are displaced only in the longitudinal direction, in the body axis system, the following relation applies

$$a_{n,cg} = a_{n,i} - \frac{x}{g}\left(\ddot{\theta} - \dot{\psi}\dot{\phi}\right) \tag{1}$$

where x is the distance from the center of gravity to the accelerometer. The product of the two angular velocities was small compared with the pitch acceleration; therefore, equation (1) becomes

$$a_{n,cg} = a_{n,i} - \frac{x}{g}\ddot{\theta} \tag{2}$$

and

$$C_N = \frac{W/S}{q} a_{n,cg} \tag{3}$$

Likewise,

$$a_{t,cg} = a_{t,i} - \frac{x}{g}\left(\ddot{\psi} - \dot{\theta}\dot{\phi}\right) \tag{4}$$

and

$$C_Y = \frac{W/S}{q} a_{t,cg} \tag{5}$$

Similarly,

$$a_{l,cg} = a_{l,i} + \frac{x}{g}\left(\dot{\theta}^2 + \dot{\psi}^2\right) \tag{6}$$

and

$$C_A = \frac{W/S}{q} a_{l,cg} \tag{7}$$

The normal force plotted against the transverse force indicated that the roll rate was small and essentially constant and that the trim center was near the origin. Therefore, the total normal force calculated from equations (3) and (5) is

$$C_{N,tot} = \pm\sqrt{C_N{}^2 + C_Y{}^2} \tag{8}$$

Moment Coefficients

The model had two planes of symmetry and a small roll rate compared with the angular acceleration; therefore, the equations for the pitching- and yawing-moment coefficients can be expressed as follows:

$$C_m = \frac{I_Y}{qSd} \ddot{\theta} \tag{9}$$

$$C_n = \frac{I_Z}{qSd} \ddot{\psi} \tag{10}$$

The moments of inertia were determined by swinging the model as a simple pendulum. The total pitching-moment coefficient calculated from equations (9) and (10) is

$$C_{m,tot} = \pm\sqrt{C_m{}^2 + C_n{}^2} \tag{11}$$

The method of reducing measured flight accelerations to force and moment coefficients is discussed in detail in references 10 and 11. The procedure was employed in the investigation of two bluff shapes in reference 12.

Angle of Attack

The pitching acceleration was measured by two normal accelerometers displaced along the longitudinal axes. With one accelerometer in the

nose and the other near the center of gravity the pitching acceleration will be given by (see eq. (15) of ref. 10)

$$\ddot{\theta} = \frac{g\left(a_{n,nose} - a_{n,cg}\right)}{\left(x_{n,nose} - x_{n,cg}\right)} \tag{12}$$

Similarly,

$$\ddot{\psi} = \frac{g\left(a_{t,nose} - a_{t,cg}\right)}{\left(x_{t,nose} - x_{t,cg}\right)} \tag{13}$$

Plots of $\ddot{\theta}$ against $\ddot{\psi}$ indicate the total motion was essentially planar. Therefore,

$$\ddot{\theta}_{tot} = \ddot{\theta} \sin \epsilon + \ddot{\psi} \cos \epsilon \tag{14}$$

and

$$\ddot{\psi}_{tot} = \ddot{\theta} \cos \epsilon + \ddot{\psi} \sin \epsilon \tag{15}$$

where ϵ is the angular orientation of the total pitch plane. The value of $\ddot{\theta}_{tot}$ was large compared with the value of $\ddot{\psi}_{tot}$ and the change in the flight-path angle was essentially zero for the test time. Therefore, the angle of attack was calculated by the successive integrations

$$\dot{\theta}_{tot} = \int_{t_1}^{t_2} \ddot{\theta}_{tot}\, dt + C_1 = \dot{\alpha} \tag{16}$$

and

$$\alpha = \int_{t_1}^{t_2} \dot{\theta}\, dt + C_2 \tag{17}$$

The angle of attack was also determined by integrating equations (12) and (13) separately, adding the two angular velocities vectorially, and integrating a second time to obtain the angle. The two methods produced the same result.

The variation of the axial-force, total normal-force, and total pitching-moment coefficients with the angle of attack was obtained from the time histories of the respective quantities.

RESULTS AND DISCUSSION

Roll Rate and Trim

The variation of the normal-force coefficient with respect to the transverse-force coefficient is shown in figure 6. Each loop represents the variation of these coefficients as the model oscillates through one-half of a cycle. The outside loops indicate that the model was below roll resonance. (See ref. 11.) The angle between rays drawn from the center of each loop to the approximate trim center is the change of the roll angle for one pitching oscillation. The plot is representative of the conditions prevailing during the test flight. The average roll rate was about 0.32 radian per second for the entire test flight. No rapid increase or decrease occurred at any time. In the analysis procedure the trim center was considered to be at the origin.

Angle of Attack

Figure 7 presents the variation of the angular pitching acceleration with respect to the angular yawing acceleration. The Mach number range for figure 7(a) is 2.62 to 2.13 and for figure 7(b), 1.14 to 1.11. The two motions were resolved into two vectors, $\ddot{\theta}_{tot}$ and $\ddot{\psi}_{tot}$. The vector along the $\ddot{\theta}_{tot}$ axis in figures 7(a) and 7(b) represents the total pitching acceleration, and the vector parallel to the $\ddot{\psi}_{tot}$ axis represents the total yawing acceleration. The time histories of the angular accelerations are shown in figure 8(a) for M = 2.62 to 2.13 before the resolution. Figure 8(b) shows the time history of the total pitching acceleration and the total yawing acceleration. The result of integrating the in-plane component successively to obtain the total pitching velocity and angle of attack is shown as the solid curve of figures 8(c) and 8(d). The points with symbols indicate times when the pitching velocity and angle of attack should be zero; that is, the angle of attack should be zero when the total pitching acceleration is zero and the total pitching velocity should be zero when the angle of attack is a maximum. The dashed curves represent the corrected quantities. The integration procedure showed that the model did not tumble but oscillated through large angles of attack after separation from the launch vehicle. The angles ranged from about $\pm 160^{\circ}$ at the separation Mach number of 2.62 to about $\pm 140^{\circ}$ at a Mach number of 1.11.

Normal Force and Axial Force

The variation of the total normal-force and axial-force coefficients is shown in figures 9(a) to 9(d). The curves of the total normal force

indicate that the slope between $\alpha = 0^\circ$ and 10° is positive and increases with increasing Mach number. The maximum normal force occurs between $\alpha = 115^\circ$ and 135° throughout the test Mach number range. The axial force is a maximum between $\alpha = 0^\circ$ and 10° and increases slightly with increasing Mach number. The minimum axial force occurs near $\alpha = 80^\circ$ for all Mach numbers. In general, the trends are consistent with the results of references 3 and 6.

Stability

The pitching-moment curves of figures 9(a) to 9(d) show that the model trim center was near an angle of attack of 0°. This trend would be expected since the model had geometric and mass symmetry. The average slopes between $\alpha = 0^\circ$ and 10°, for $M = 2.62$ to 1.54, and $\alpha = 0^\circ$ and -10°, for $M = 1.13$ to 1.11, exhibit the same trend as those of references 3 and 6 at $\alpha = 0^\circ$. That is, the static stability increases with increasing Mach number. The model was statically stable about the trim point for all Mach numbers and angles of attack.

Comparison With Wind-Tunnel Data

In figure 10 the normal-force coefficient, axial-force coefficient, and center of pressure are compared with the wind-tunnel data of references 3 and 6. The flight model and the two wind-tunnel models had about the same ratio of total length to maximum diameter but different afterbody shapes which affect the normal-force and center-of-pressure results at angles of attack greater than 30° and the axial-force results at angles greater than 80°.

Figure 10(a) indicates good agreement of the normal force for the flight model and the model of reference 3. The model of reference 6 shows a larger normal force for angles greater than 30° indicating, as would be expected, a greater contribution to the total normal force by the afterbody with increasing angle of attack.

Figure 10(b) shows the center-of-pressure location, rearward from the geometric center of the large blunt nose, in percent of the maximum diameters of the respective models. The more rearward location of the center of pressure of the model of reference 6 than that of the flight model is consistent with the increased afterbody lift effectiveness noted previously.

In general, the comparison shows that the change in center of pressure with angle of attack was similar for the flight model and reference models, except for the model of reference 6, below $\alpha = 25^\circ$. Below

$\alpha = 20^{\circ}$ the normal force is very small so that a small change in normal force will cause a large change in the center-of-pressure location. This effect is indicated by the sudden shift rearward of the center of pressure of the model of reference 6. The model of reference 3 had a larger face-shape ratio (ratio of maximum diameter to twice the radius of the spherical face) which would move the center of pressure slightly further rearward of the center of gravity (see ref. 8).

Figure 10(c) indicates the three models had essentially the same drag characteristics. The test Reynolds number differed for each of the three models, but references 3 and 6 indicate little or no change in the axial-force and normal-force coefficients with a Reynolds number change.

L
1
2
3
0

CONCLUSIONS

The results of an investigation to determine whether a small-scale model of a reentry spacecraft configuration in free flight would recover from an intentionally induced tumbling motion indicate the following conclusions:

1. The model rotated to its stable position with the blunt nose forward and continued to oscillate through large angles of attack ranging from $\pm 160^{\circ}$ at a Mach number of 2.62 to $\pm 140^{\circ}$ at a Mach number of 1.11.

2. The model was statically stable about the trim point for all test Mach numbers and angles of attack.

3. The maximum normal force occurs between angles of attack of 115° and 135°, and the minimum axial force occurs near an angle of attack of 80°.

Langley Research Center,
National Aeronautics and Space Administration,
Langley Air Force Base, Va., September 20, 1961.

REFERENCES

1. Scallion, William I.: Full-Scale Wind-Tunnel Investigation of the Low-Speed Static Aerodynamic Characteristics of a Model of a Reentry Capsule. NASA TM X-220, 1959.

2. Pearson, Albin O.: Wind-Tunnel Investigation at Mach Numbers From 0.50 to 1.14 of the Static Aerodynamic Characteristics of a Model of a Project Mercury Capsule. NASA TM X-292, 1960.

3. Shaw, David S., and Turner, Kenneth L.: Wind-Tunnel Investigation of Static Aerodynamic Characteristics of a 1/9-Scale Model of a Project Mercury Capsule at Mach Numbers From 1.60 to 4.65. NASA TM X-291, 1960.

4. Penland, Jim A., and Armstrong, William O.: Preliminary Aerodynamic Data Pertinent to Manned Satellite Reentry Configurations. NACA RM L58E13a, 1958.

5. Carter, Howard S., Kolenkiewicz, Ronald, and English, Roland D.: Principal Results From Wind-Tunnel Stability Tests of Several Proposed Space Capsule Models up to an Angle of Attack of 33°. NASA TM X-21, 1959.

6. Turner, Kenneth L., and Shaw, David S.: Wind-Tunnel Investigation at Mach Numbers From 1.60 to 4.50 of the Static-Stability Characteristics of Two Nonlifting Vehicles Suitable for Reentry. NASA MEMO 3-2-59L, 1959.

7. Johnson, Joseph L., Jr.: Wind-Tunnel Investigation at Low Subsonic Speeds of the Static and Oscillatory Stability Characteristics of Models of Several Space Capsule Configurations. NASA TM X-285, 1960.

8. Smith, Fred M.: A Wind-Tunnel Investigation of the Aerodynamic Characteristics of Bodies of Revolution at Mach Numbers of 2.37, 2.98, and 3.90 at Angles of Attack to 90°. NASA TM X-311, 1960.

9. Blanchard, Willard S., Jr., and Hoffman, Sherwood: Full-Scale Flight Test of a Proposed Abort-Escape System for a Manned Space Capsule From Sea Level. NASA TM X-351, 1960.

10. Gillis, Clarence L., and Mitchell, Jesse L.: Determination of Longitudinal Stability and Control Characteristics From Free-Flight Model Tests With Results at Transonic Speeds for Three Airplane Configurations. NACA Rep. 1337, 1957.

L 1 2 3 0

11. Nelson, Robert L.: The Motions of Rolling Symmetrical Missiles Referred to a Body-Axis System. NACA TN 3737, 1956.

12. Coltrane, Lucille C.: Investigation of Two Bluff Shapes in Axial Free Flight Over a Mach Number Range From 0.35 to 2.15. NACA RM L58A16, 1958.

Figure 1.- Diagram of the body axis system.

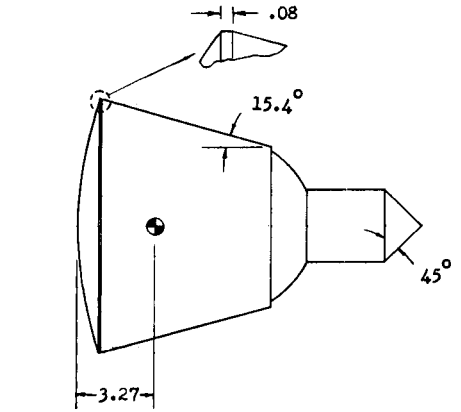

Top view

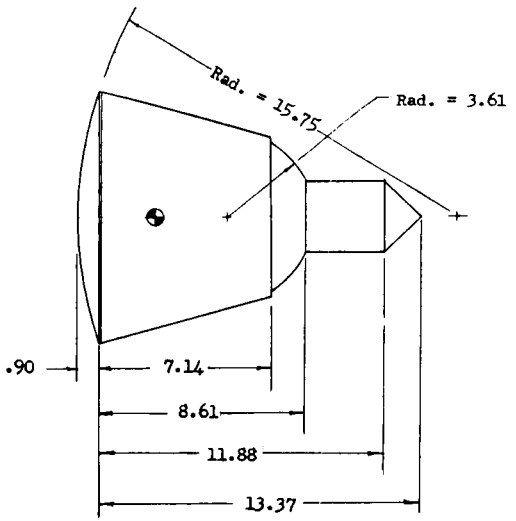

Side view

Model Characteristics:

$W = 70.5$ lb

$I_Y = I_Z = 0.19$ slug-ft^2

$I_X = 0.08$ slug-ft^2

$S = 0.601$ sq ft

$d = 10.5$ in.

$\frac{x_{cg}}{d} = 0.311$

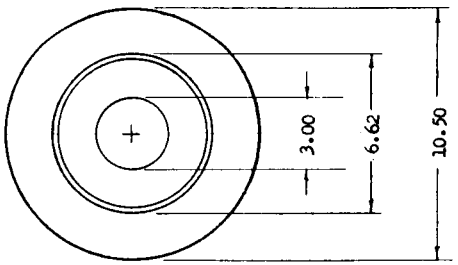

Rear view

Figure 2.- Three-view drawing of the spacecraft model. All dimensions are in inches.

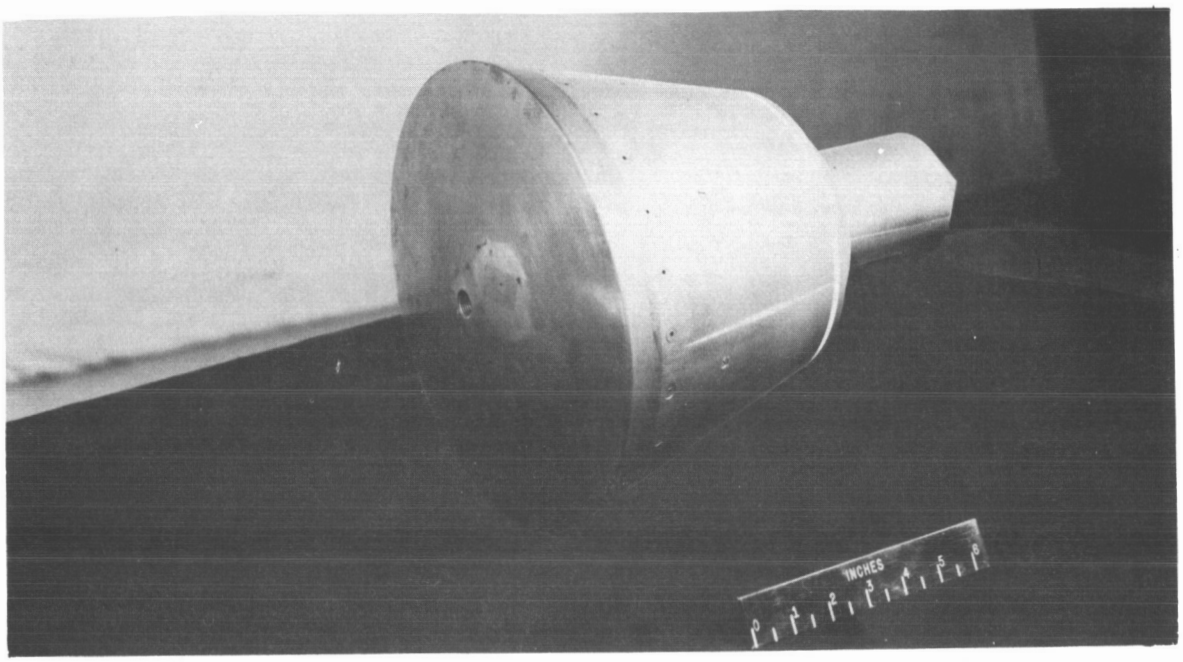

(a) Three-quarter front view.

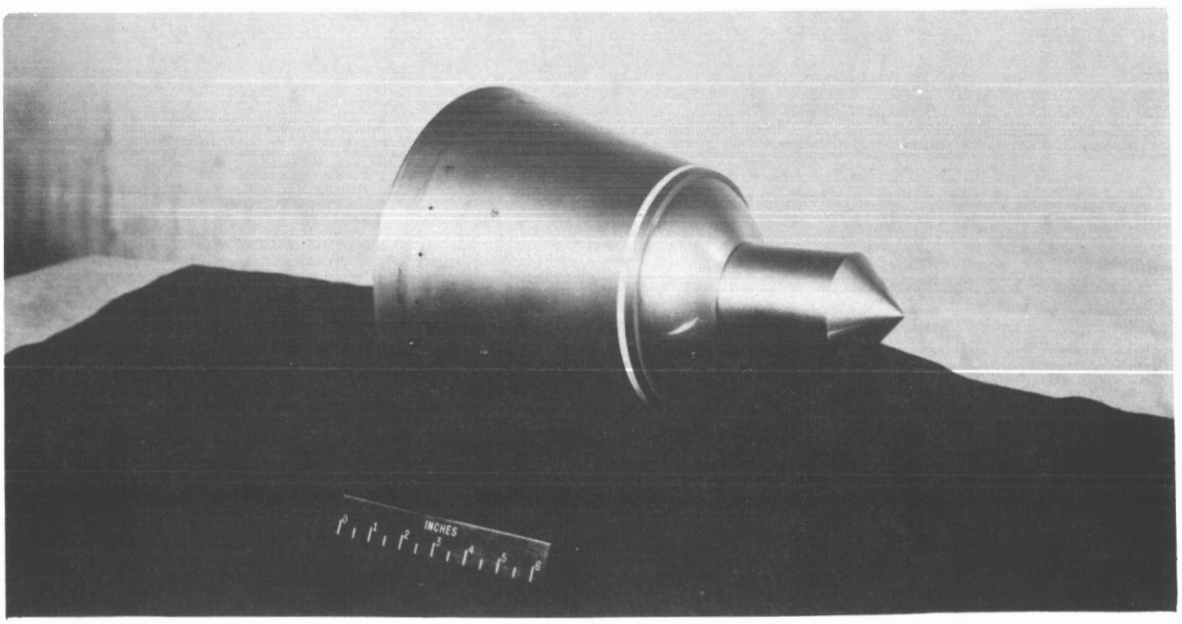

(b) Three-quarter rear view. L-61-5110

Figure 3.- Photographs of model.

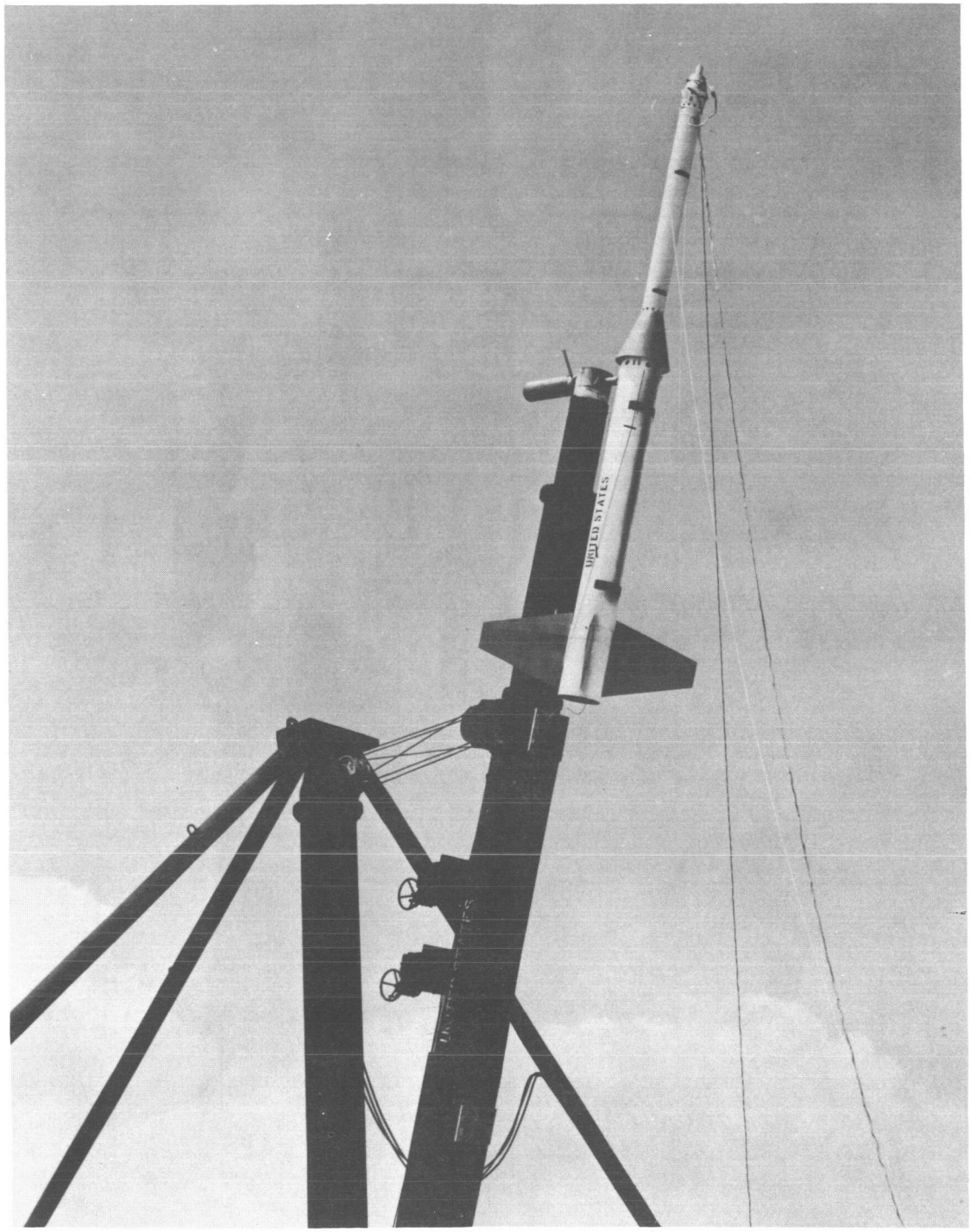

L-59-4316

Figure 4.- Model and launch vehicle on launcher at an angle of elevation of 70°.

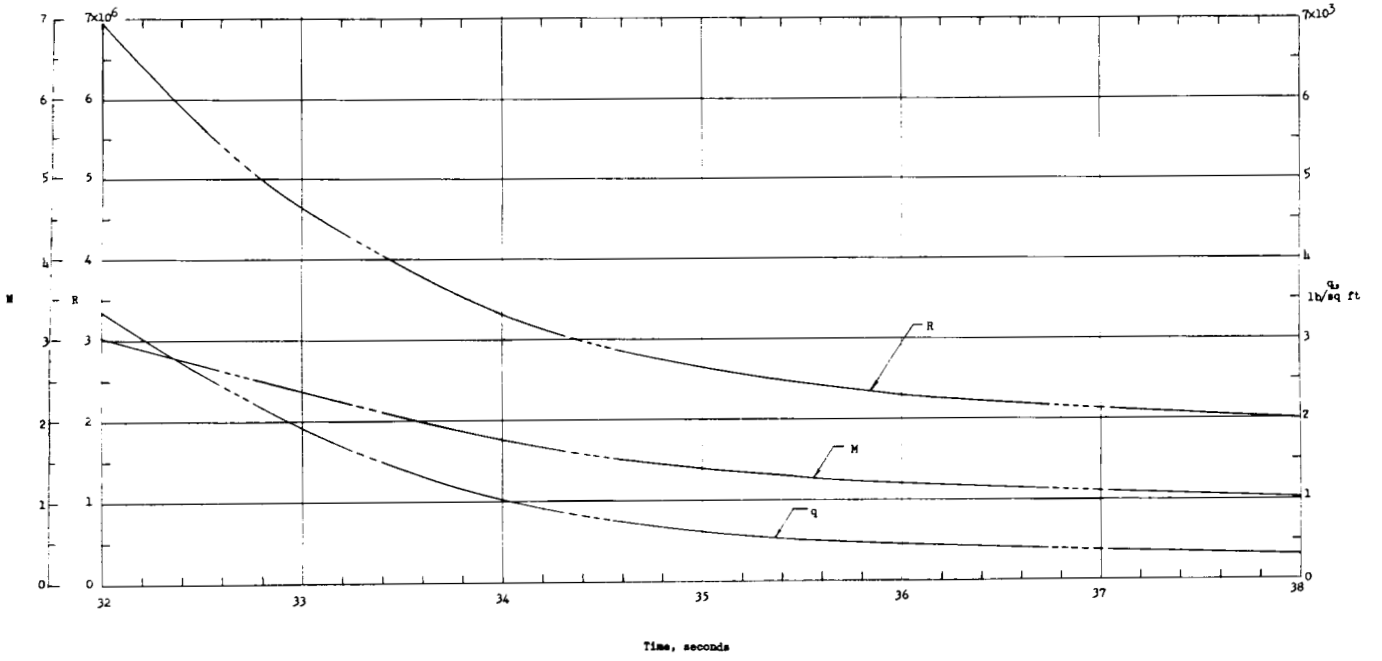

Figure 5.- Variation of test Reynolds number, Mach number, and dynamic pressure with time. Dashed portion of curves indicate data analysis intervals.

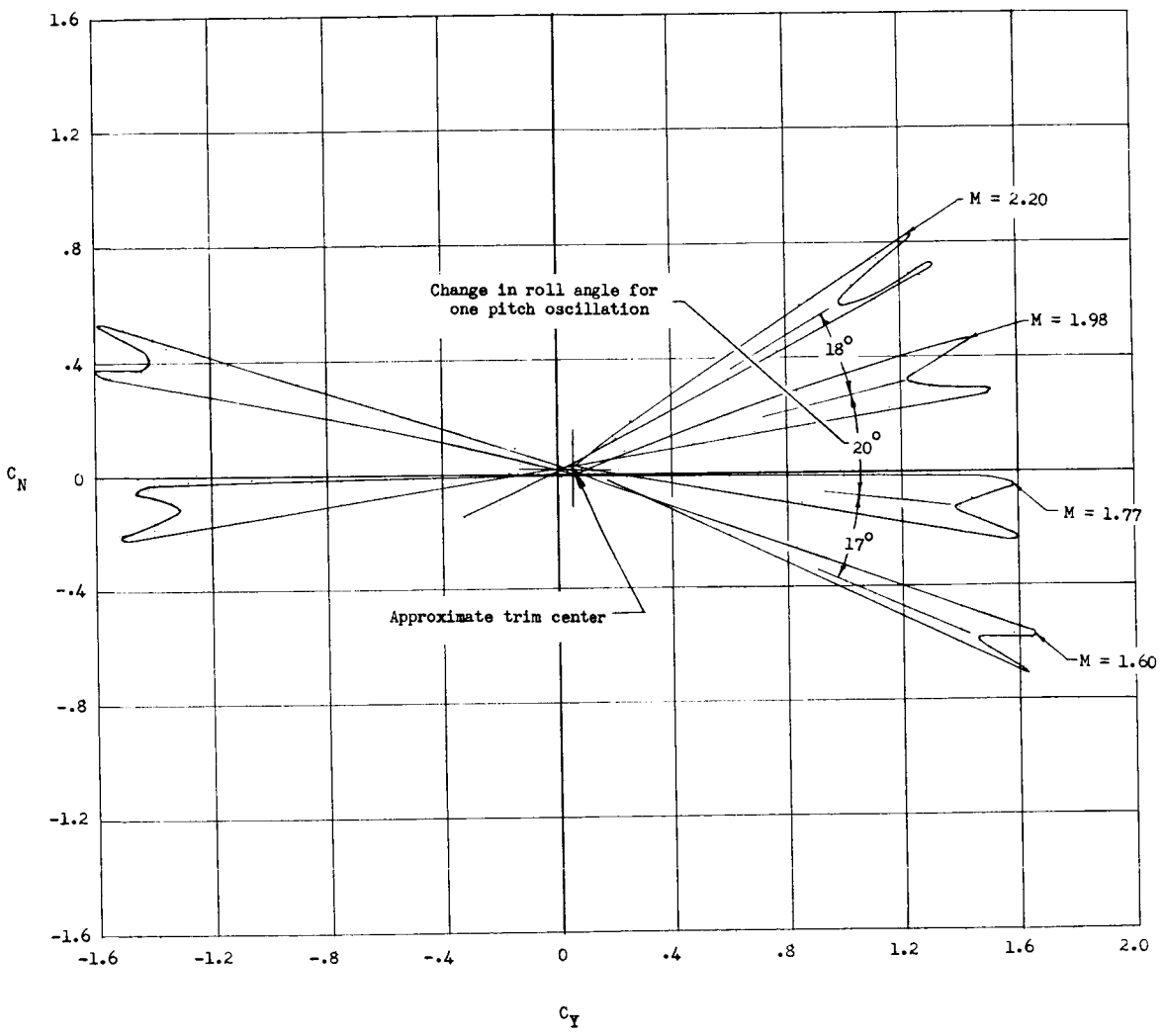

Figure 6.- Variation of normal-force coefficient with side-force coefficient for initial oscillations.

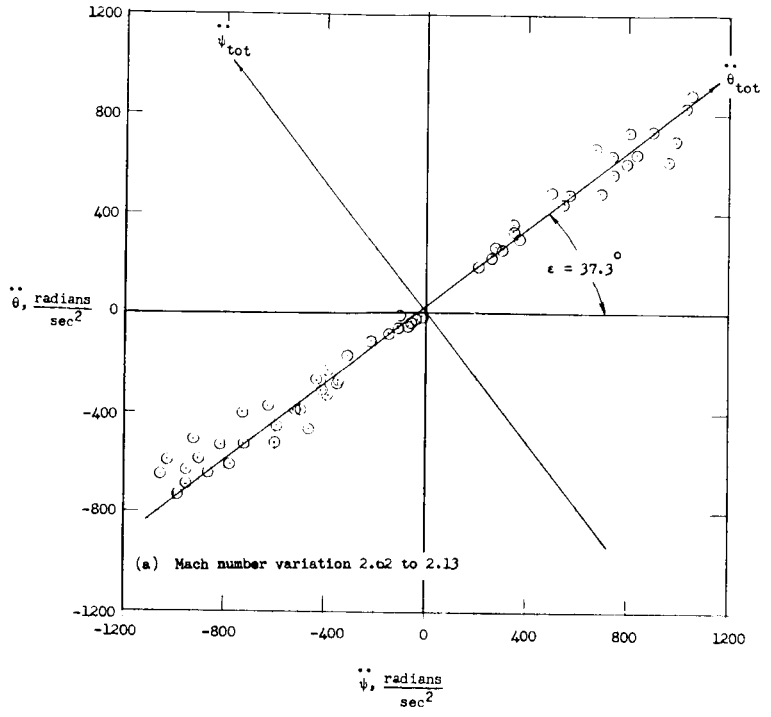

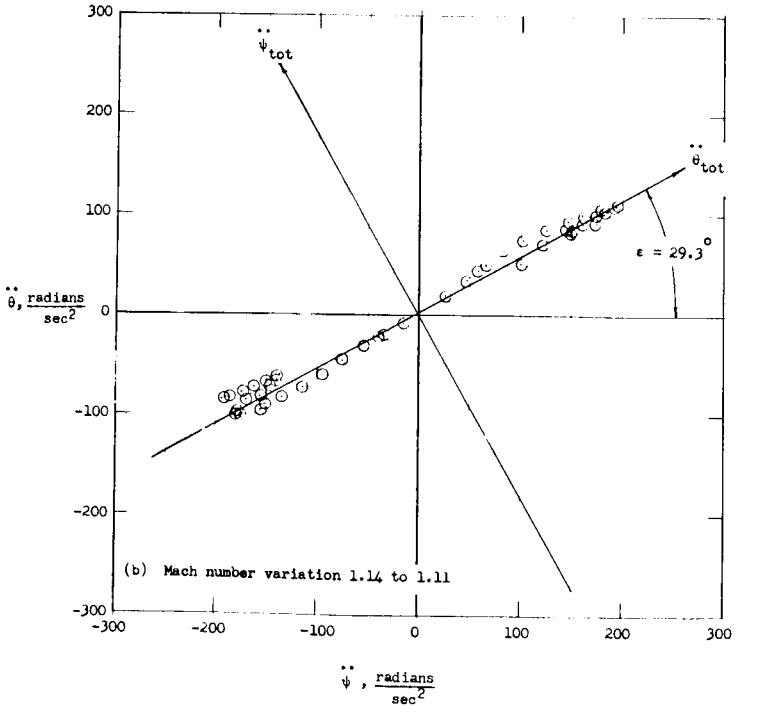

Figure 7.- Variation of pitching acceleration with yawing acceleration.

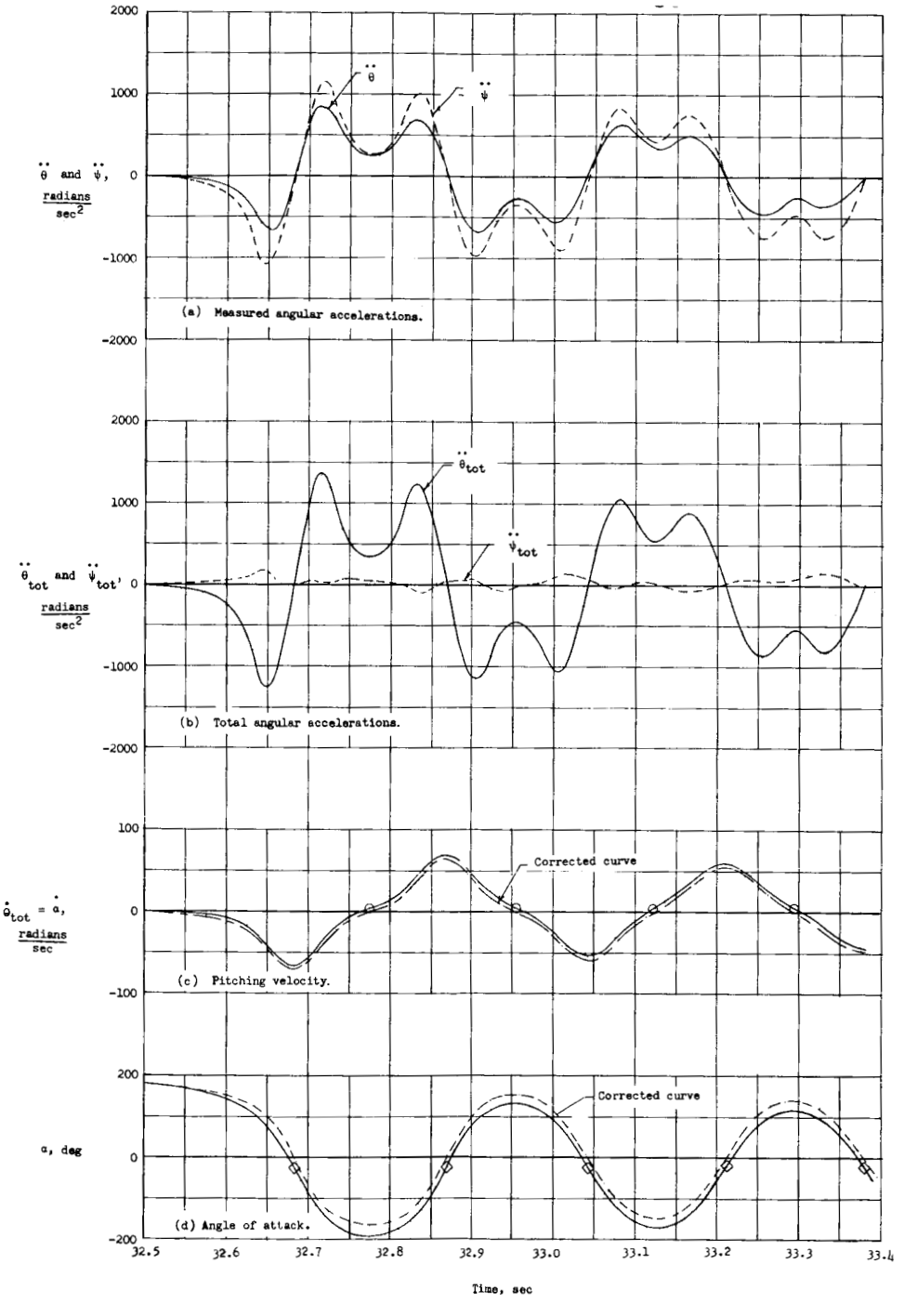

Figure 8.- Time history of the measured angular accelerations and the quantities obtained by continuous integration at Mach numbers from 2.62 to 2.13.

[redacted]

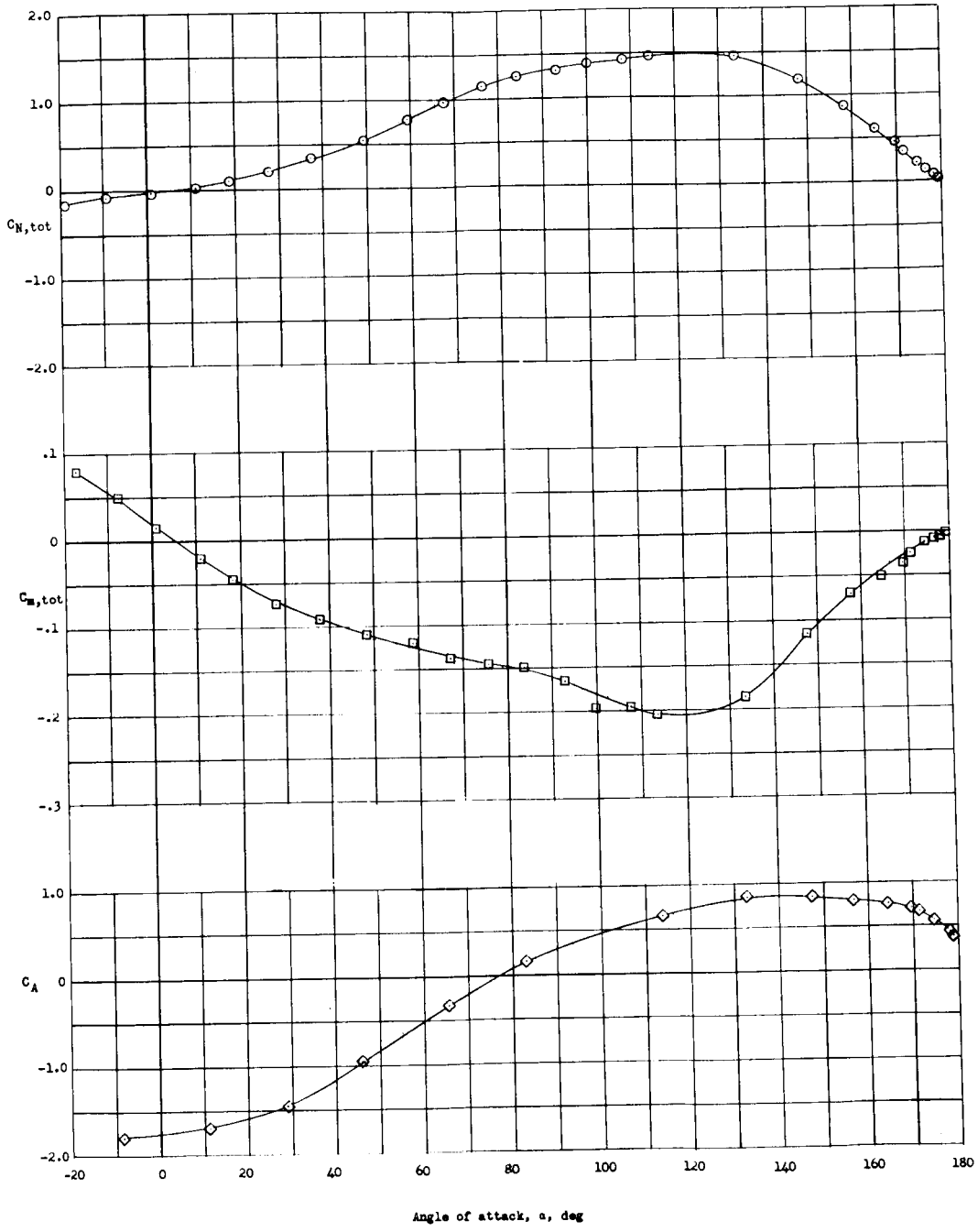

(a) Mach number range from 2.62 to 2.52.

Figure 9.- Variation of the normal-force, pitching-moment, and axial-force coefficients with the angle of attack.

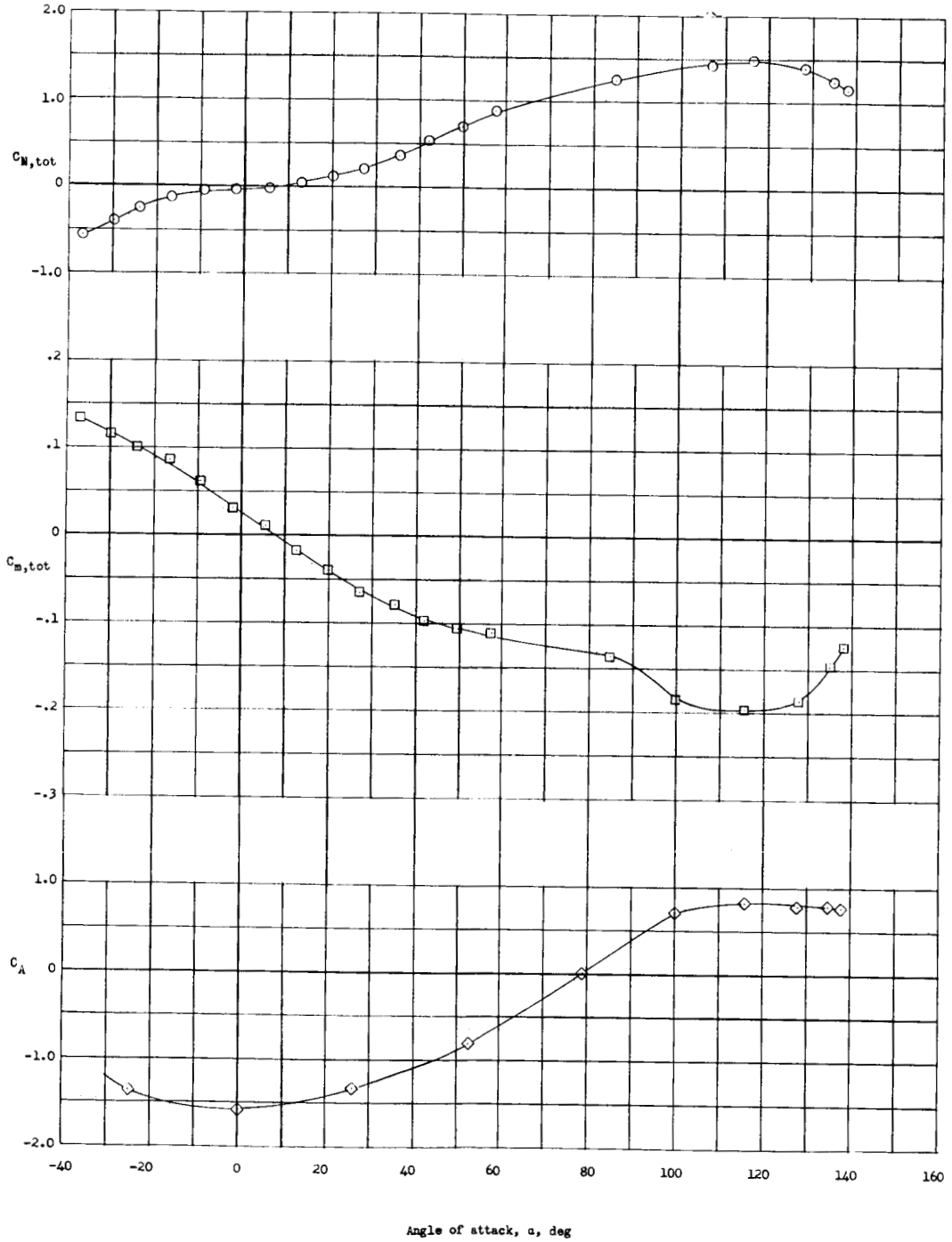

(b) Mach number range from 2.18 to 2.13.

Figure 9.- Continued.

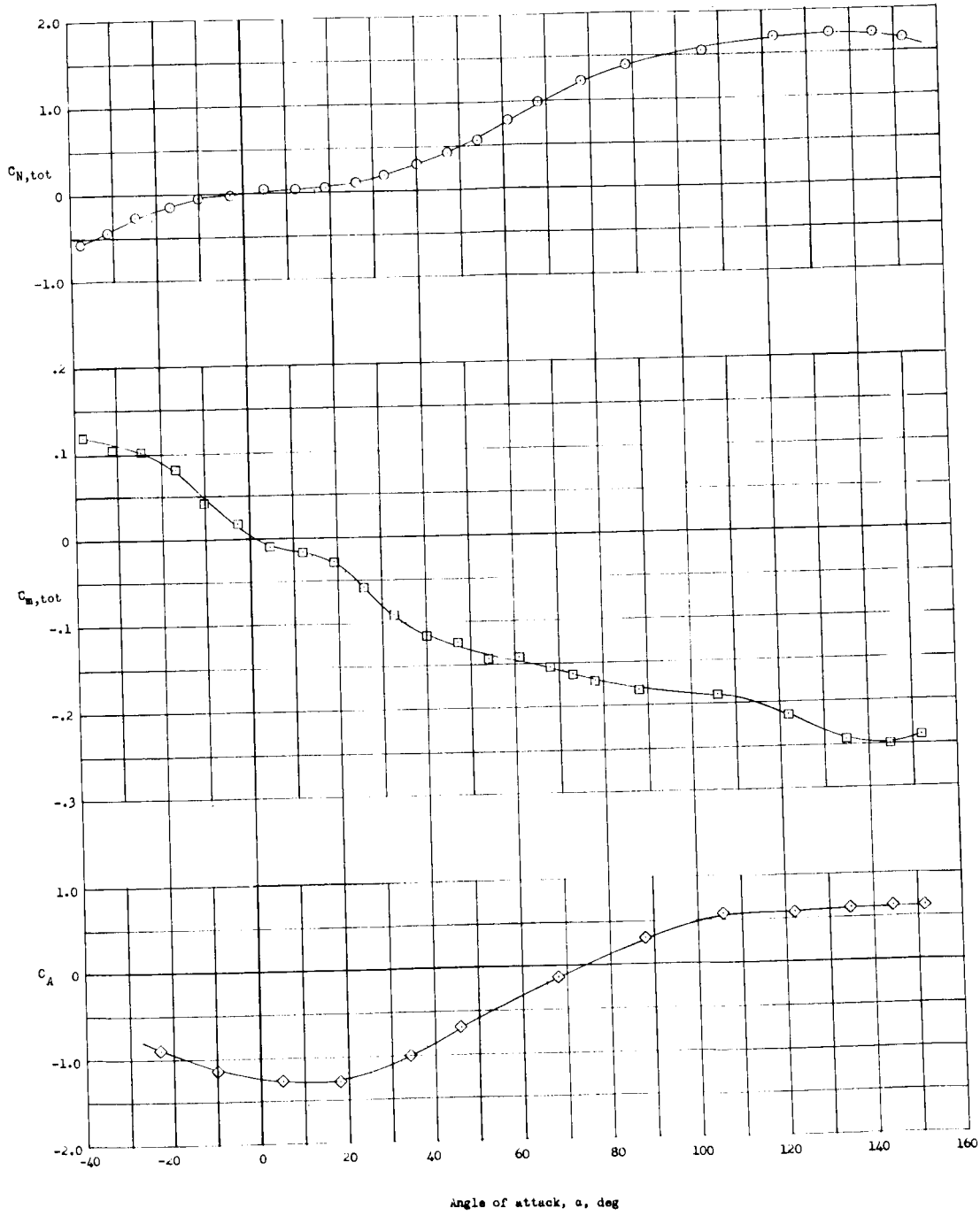

(c) Mach number range from 1.60 to 1.54.

Figure 9.- Continued.

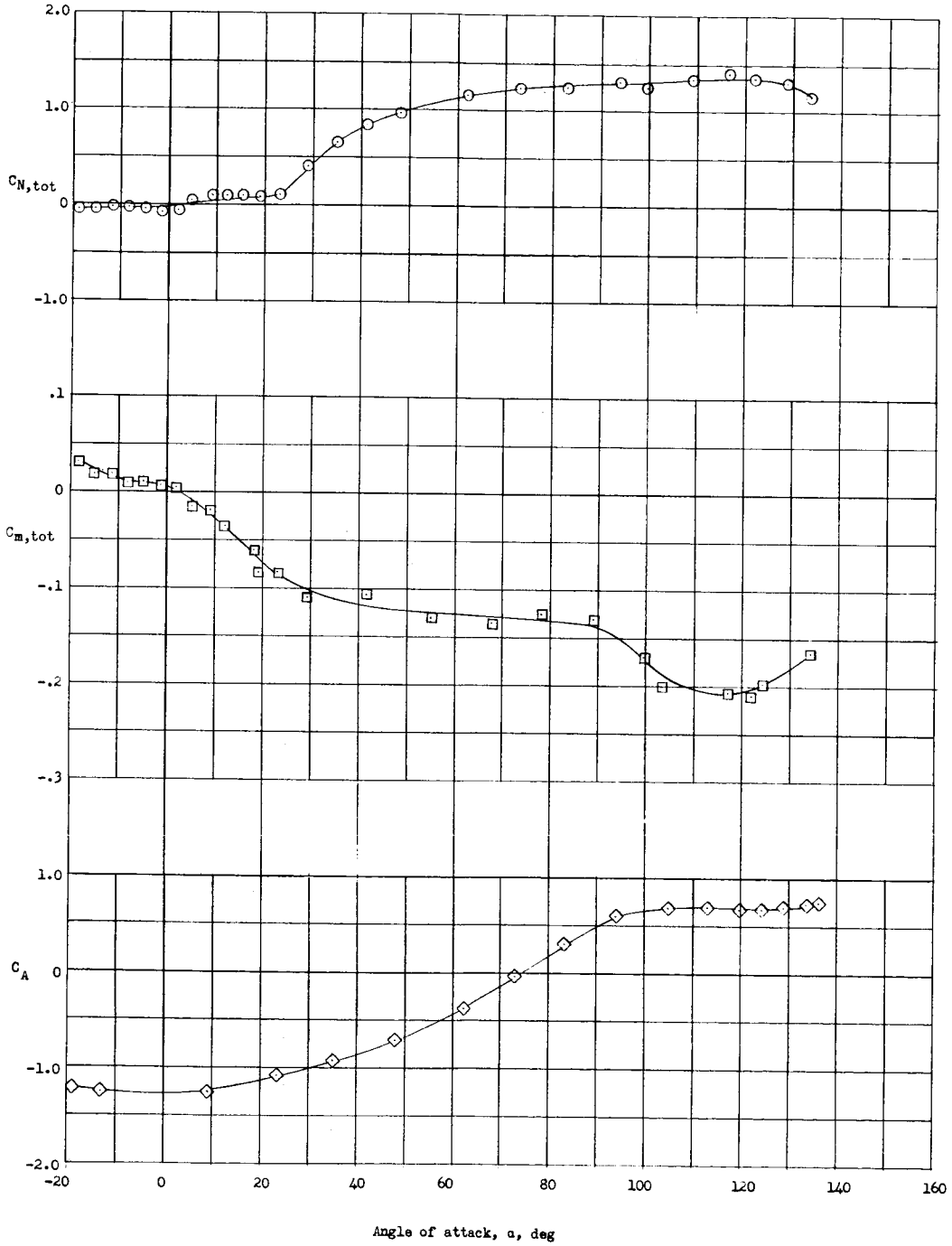

(d) Mach number range from 1.13 to 1.11.

Figure 9.- Concluded.

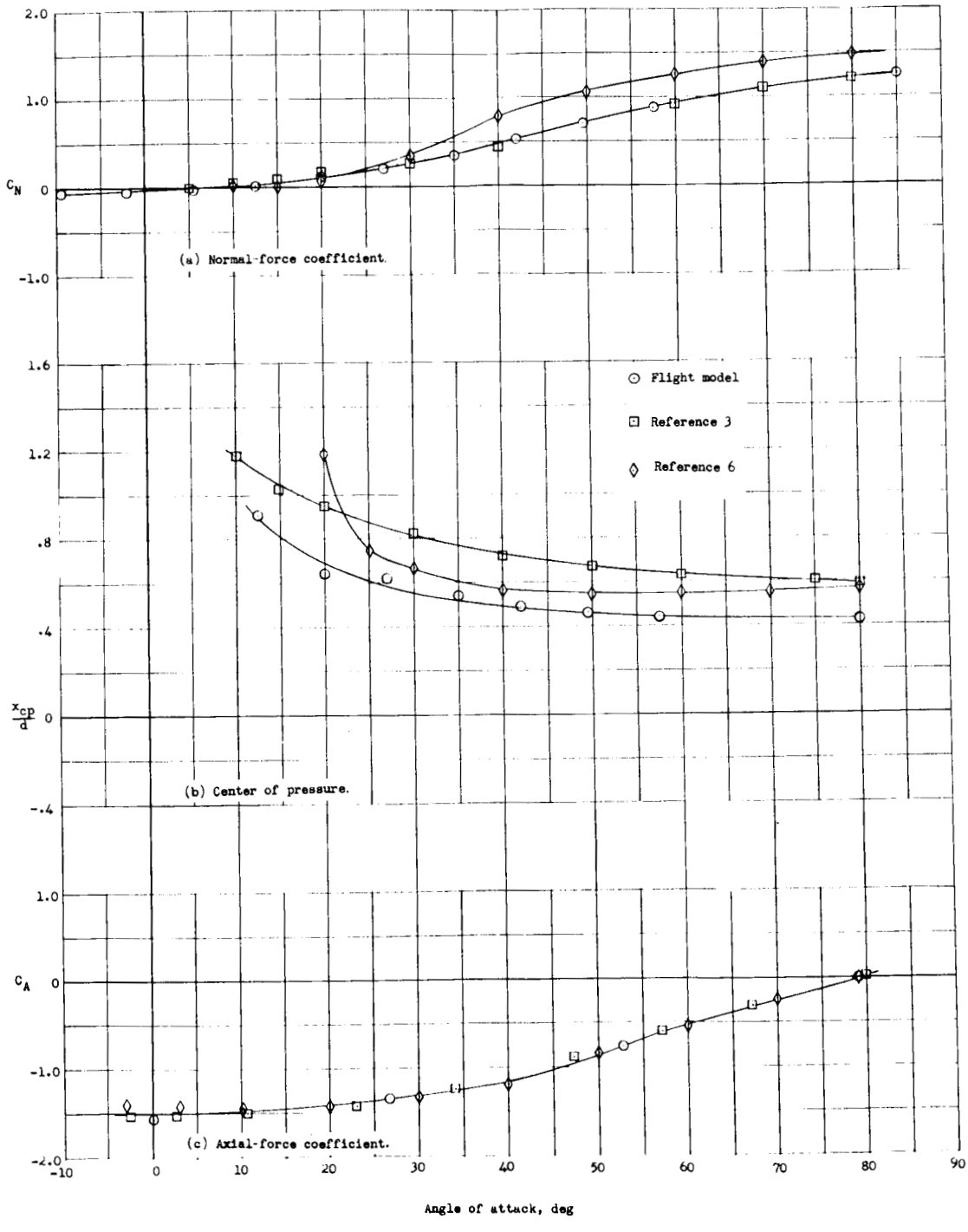

Figure 10.- Comparison of flight model results with wind-tunnel data at a Mach number of 2.06.

L-1230